Characterization and Modeling of the High Temperature Flow Behavior of Aluminum Alloy 2024

P. L. CHARPENTIER, B. C. STONE, S. C. ERNST, and J. F. THOMAS, Jr.

Isothermal flow curves were determined for aluminum alloy 2024-0 at temperatures of 145 to 482 °C and at constant true-strain rates of 10^{-3} to 12.5 s^{-1} using compression tests of cylindrical specimens. The average pressure was corrected for friction and for deformation heating to determine the flow stress. At 250 °C and above, the isothermal flow curves usually exhibited a peak followed by flow softening. At 145 °C the flow curves exhibited strain hardening. For 250 °C $\leqq T \leqq$ 482 °C, 10^{-3} $s^{-1} \leqq \dot{\varepsilon} \leqq 12.5$ s^{-1}, and $\varepsilon \leqq 0.6$ the flow behavior was represented by the constitutive equation $\sigma = K\ (T, \varepsilon)\dot{\varepsilon}^{m(T,\varepsilon)}$ where log K and m are simple functions of temperature and strain. The as-deformed microstructures generally supported the idea that flow softening in Al 2024-0 is caused by dynamic recovery. At the higher temperatures and strain rates, however, fine recrystallized grains were observed in local areas near second phase particles and at as-annealed grain boundaries. At 482 °C, there was evidence of re-dissolution of the $CuMgAl_2$ precipitate.

I. INTRODUCTION

PROGRESS in deformation processing technology depends both on advanced process modeling techniques (*e.g.*, finite element methods) and on precise characterization of the flow behavior of the workpiece material under conditions of temperature and strain rate representative of the process. Equations describing the strain, strain rate, and temperature dependence of the flow stress are required as input to computer process models to predict the deformation history of any material element during forming. These predictions, when combined with proper processing—microstructure relationships and with failure criteria for the material, can help in defining and optimizing processing conditions to produce defect-free parts with controlled dimensions, microstructures, and mechanical properties.

This overall approach has been actively pursued in recent years for aircraft and aerospace materials and is currently being further developed. Initially, the approach was applied to the design of a forging process capable of producing a titanium alloy (Ti-6-2-4-2) turbine engine compressor disk with different microstructures, and therefore different mechanical properties, in the bore and in the rim regions (dual-property disk).[1] In the bore region, where high strength and long low-cycle fatigue life is required, an equiaxed (α/β) structure was produced; in the rim region, an acicular (α/β) structure was produced to give good creep resistance. The approach is now being extended and refined[2] to include temperature effects, more complex shapes (*e.g.*, 3D forgings), and different alloys (*e.g.*, Ti-10-2-3, Al-2024 with and without addition of refractory fibers). Also, processing maps are being developed which not only delineate "safe" processing regions of strain rate, $\dot{\varepsilon}$, and temperature, T, to avoid fracture[3] but help define optimum conditions of $\dot{\varepsilon}$ and T to obtain desired microstructures.[4]

The objectives of the present work were to characterize the flow behavior of aluminum alloy 2024, produced by ingot metallurgy, over a relatively broad range of temperatures and strain rates (145° to 482 °C, 10^{-3} to 12.5 s^{-1}) and to examine the microstructures resulting from these processing conditions. In spite of its wide use for structural applications in airframes, flow stress data on Al-2024 for the above temperatures and strain rates appear limited in the open literature. However, such data are of value not only of themselves but also to bring out differences in behavior between ingot-metallurgy (IM) Al-2024 and rapidly solidified, powder-metallurgy (PM) Al-2024 which is of current interest. Because of the rapid solidification rate, finer second phase particles and new phases can be present in (PM) Al-2024 which cause different dynamic metallurgical processes to occur during hot forming and can result in different mechanical properties. For example, it is generally accepted that dynamic recovery, rather than dynamic recrystallization, occurs in (IM) Al-2024 due to the high stacking-fault energy and easy cross-slip. By contrast, dynamic recrystallization has been observed in rapidly solidified (PM) Al-2024.[5]

II. EXPERIMENTAL PROCEDURE

A. *Material*

The Al-2024 alloy was received from Battelle Columbus Laboratories in the form of a 114 mm (4.5 in.) diameter billet which had been processed by hot rolling followed by press forging and then heat treated to produce the T351 temper. The chemical composition of the alloy (in weight pct) was 4.9 Cu, 1.8 Mg, 0.9 Mn, 0.25 Zn, 0.5 Fe, 0.5 Si, and balance Al. The as-received microstructure (Figure 1) consisted of large, elongated grains (typical length and width of 5 mm and 50 μm, respectively) and contained alignments of large, round particles of composition (Cu, Al) as well as massive inclusions with angular shapes, probably

P. L. CHARPENTIER, formerly Visiting Associate Professor, Wright State University, Dayton, OH 45435, is Metallurgical Consultant, 909 Ruth Street, Pittsburgh, PA 15243. B. C. STONE, formerly a Mechanical Systems Engineering Student at Wright State University, is Research Specialist, Mead Corporation, Miamisburg, OH. S. C. ERNST, formerly a Materials Engineering Student at Wright State University, is Graduate Student, Department of Welding Engineering, The Ohio State University, Columbus, OH. J. F. THOMAS, Jr., formerly Director, Metallurgy Program, National Science Foundation, Washington, DC, is Professor and Chairman, Mechanical Systems Engineering Department, Wright State University, Dayton, OH 45435.

Manuscript submitted October 20, 1984.

(Cu, Fe, Mn) Al_6. Elements present in particles and inclusions were determined by energy-dispersive X-ray analysis in the scanning electron microscope.

Cylindrical specimens with a diameter D = 12.7 mm (0.5 in.) and a height h = 19.8 mm (0.78 in.) were machined from the billet with their longitudinal axes parallel to the axis of the billet. These specimens were annealed to produce the 0 temper before compression testing. The anneal consisted of 1 hour 35 minutes between 410 °C and 425 °C, the maximum temperature reached. The specimens remained at 425 °C for 40 minutes, were furnace cooled to 255 °C at an average cooling rate of 28 °C/hr., and then air cooled to room temperature. The resulting microstructure (Figure 2) had essentially the same grain size as the as-received material, but a coarse, uniformly distributed precipitate of $CuMgAl_2$ was present within the grains and at the grain boundaries. Precipitate-free zones were noted along the grain boundaries and near the alignments of (Cu, Al) particles.

B. *Compression Tests*

The specimens were coated with a water-based graphite lubricant (Deltaforge 182) applied as recommended by the manufacturer (Acheson Colloids Company). Constant true strain rate compression tests were performed in a Dake servo-hydraulic press ($\dot{\varepsilon}$ = 10^{-3} to 10^{-1} s^{-1}) or an MTS servohydraulic tester ($\dot{\varepsilon}$ = 1 and 12.5 s^{-1}), both equipped with superalloy compression tooling and a specially designed electrical RC circuit to provide an exponential time-decay of the ram velocity.[6,7] Tests were conducted at nominal temperatures of 145°, 250°, 365°, 425°, and 482 °C and at nominal true strain rates of 10^{-3}, 10^{-2}, 10^{-1}, 1, and 12.5 s^{-1}. The actual true strain rates differed from the nominal true strain rates by approximately 5 pct, on average. The heating procedure consisted of bringing the superalloy compression tooling situated in the center of a resistance furnace to the desired test temperature, inserting the specimen between the compression platens, which caused the temperature of the platens to drop, and waiting a sufficient time for the test temperature to be reached in the specimen and reestablished in the platens. The temperature was monitored by a thermocouple inserted a distance of 2 or 3 mm into the midplane of the specimen for the tests conducted on the MTS machine and by two thermocouples embedded in the center of each compression platen, 2 mm below the surface, for the tests performed on the Dake press. Five- to ten-minute soak times at temperature were allowed before compression in the lower temperature tests; none was allowed in the higher temperature tests (425 °C and 482 °C) to preserve the initial microstructure. Duplicate tests were run on the Dake press and the MTS machine at $\dot{\varepsilon}$ = 10^{-1}, T = 482 °C to check uniformity of results.

The specimens tested on the Dake press were compressed to a final strain, ε_f, ranging from 0.75 to 1.2 approximately, and those tested on the MTS machine to $\varepsilon_f \simeq 0.7$. However, all the flow curves for the tests run on the Dake press were truncated at a strain of ≃0.7 for analysis (in particular for the friction and temperature corrections) to avoid the effect on the flow stress of the break-down in lubrication at high strains. Also, the metallographic observations described later were made on specimens compressed to about the same final strain (0.7 to 0.8). For the tests conducted on the Dake press, companion specimens compressed to strains of 0.7 to 0.8 were used for this purpose.

Load-time curves were recorded during all the tests; displacement-time or load-displacement curves, or both, were also obtained in several tests. For most tests the stress-strain curves were obtained from the load-time records, but in some cases load-displacement records were used instead. It was verified on several tests that the two methods produced the same stress-strain curves. The displacement-time curves were used to check the constancy of the strain rate during any given test.

The temperature increase caused by deformation heating was measured or estimated for each test. For the tests run on the MTS machine, the thermocouple embedded in the specimen allowed direct measurement of the temperature increase at the end of the test. For the tests conducted on the Dake press, the temperatures of the platens were recorded

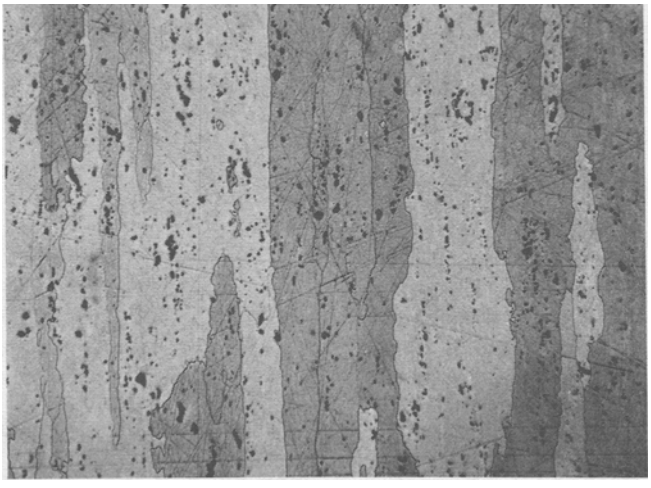

Fig. 1 — Microstructure of Al 2024-T351 (as-received condition). Magnification 74 times.

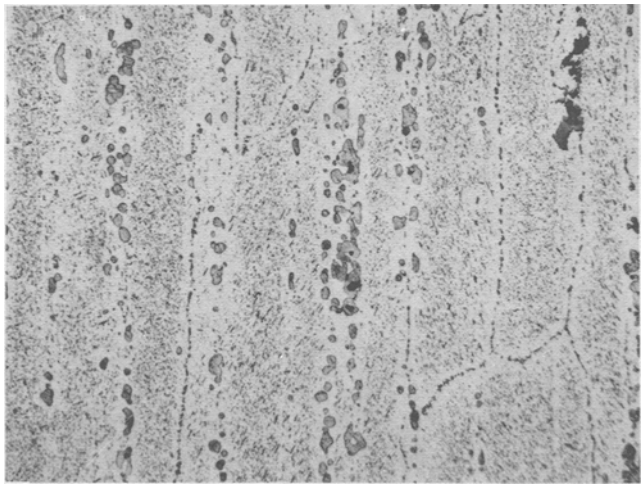

Fig. 2 — Microstructure of Al 2024-0 (as-annealed). Magnification 74 times.

throughout the test and the temperature increase of the specimen at a strain of 0.7 was estimated from the average temperature of the platens at the same strain using the specimen temperature increase during the MTS tests at 482 °C and 10^{-1} s^{-1} as a calibration. Further details are given in the section on temperature correction.

C. *Ring Friction Tests*

The ring friction test[8] is a standard method for determining the interface friction factor, f, in metalworking. Here f is defined as the ratio, $f = \tau_i/\tau_w$, of the shear strength of the interface, τ_i, to the shear strength of the workpiece, τ_w. Flat rings of dimensions OD = 25.4 mm (1.000 in.), ID = 12.7 mm (0.500 in.), and h = 8.38 mm (0.330 in.), were machined from the as-received billet, given the same anneal as the compression specimens, and coated with Deltaforge 182 graphite lubricant. The rings were compressed in the Dake press at two temperatures (250 and 425 °C) and two strain rates (10^{-3} and 10^{-1} s^{-1}) and to final axial strains ranging from −0.32 to −0.6. From the height strains and the changes in bore dimensions, values of the interface friction factor, f, were determined at these two temperatures and strain rates using standard calibration curves for the 6:3:2 ring geometry.[9] Values of f for the other temperatures and strain rates in the compression test matrix were estimated by interpolation and extrapolation, as detailed later. These f values were then used to apply a friction correction to the measured flow stress using the method described later.

D. *Metallography*

Polished and etched cross-sections were examined in the light and scanning electron microscopes before and after compression to observe the effects of temperature and rate of deformation on the resulting microstructures. Some of the as-compressed specimens examined had been quenched in ice-brine within 3 to 10 seconds of the end of compression to attempt to retain the as-deformed structures. Other specimens had only been air cooled; their microstructures would be more representative of forged parts cooled without a quench.

III. ANALYSIS, RESULTS, AND DISCUSSION

A. *Stress-Strain Curves*

The load-time records were converted to average pressure/true plastic strain data using $\varepsilon = \dot{\varepsilon}t, p = (F/A_0)\exp(\varepsilon)$, and $\dot{\varepsilon} = \varepsilon_f/t_f$, where $\dot{\varepsilon}$ = true strain rate, ε_f = final plastic strain determined from specimen height measurements before and after the test, t_f = time at the end of the test referred to the elastic loading line (Figure 3), t = time, ε = true plastic strain, p = average instantaneous pressure, F = measured load, and A_0 = initial specimen cross-section. It must be recognized that ε is the average true strain and that there are variations in strain throughout the specimen. In converting load-time records, the load oscillations due to dynamic strain aging (Portevin-Le Chatellier effect) were averaged out into a smooth curve. The point where the load-time curve deviates from the elastic line ($\varepsilon = 0$) was used to estimate the yield strength and its general trend. Yield strength values were not used in the constitutive equation analysis.

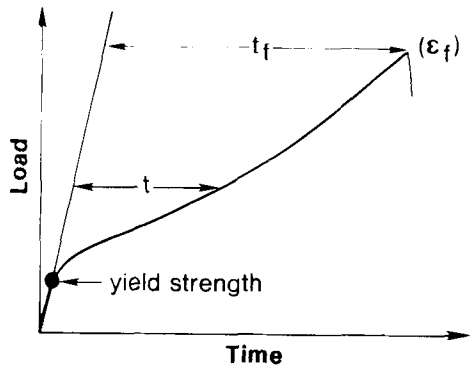

Fig. 3—Load time record. Schematic.

Friction Correction. The average pressure/true strain data were converted to true stress/true strain data using:

$$p = \sigma\left[1 + \frac{2f}{3\sqrt{3}}\frac{r_0}{h_0}\exp\left(-\frac{3\varepsilon}{2}\right)\right] \qquad [1]$$

which results from the slab analysis of the compression of a cylinder with constant interfacial friction factor, f, and a Von Mises yield surface and from integration of the local pressure over the specimen cross-sectional area. Here, r_0, h_0 = initial radius, height of the specimen, and σ = average true axial flow stress.

The values of f used in the calculations are shown in Table I. It can be seen that f decreases with increasing temperature and strain rate. The "estimated" values of f were obtained from the measured values by assuming that: (1) at constant ε, f is constant for $T \leqq 250$ °C and decreases linearly when T increases from 250 to 482 °C, and (2) at a given temperature, f decreases linearly when $\dot{\varepsilon}$ increases from 10^{-3} to 10^{-1} s^{-1} and then remains constant at the higher

Table I. Friction Factors, f, for Al-2024-0 Lubricated with Graphite and Compressed between Flat MAR-M† Dies

T (°C)	$\dot{\varepsilon} = 10^{-3}$ s^{-1}	$\dot{\varepsilon} = 10^{-2}$ s^{-1}	$\dot{\varepsilon} = 10^{-1}$ s^{-1}	$\dot{\varepsilon} = 1$ s^{-1}	$\dot{\varepsilon} = 12.5$ s^{-1}
145	0.35	0.305	0.26	—	—
250	0.35*	0.305	0.26*	—	—
365	0.24	0.21	0.175	0.175	0.175
425	0.18*	0.155	0.13*	—	—
482	0.125	0.11	0.09	0.09	0.09

*measured values, using ring tests. Each value represents the average of 2 to 4 tests. Other values are estimated by interpolation and extrapolation (see text).

†MAR-M is a trademark of Martin Marietta Company.

strain rates. As seen in Table I, f varies from 0.09 for $T = 482$ °C, $\dot{\varepsilon} = 12.5\ s^{-1}$ to 0.35 for $T = 145$ °C, $\dot{\varepsilon} = 10^{-3}\ s^{-1}$. The magnitude of the flow stress correction ranges from 3 pct for $f = 0.09$ to 11 pct for $f = 0.35$ at a strain of 0.7. The friction-corrected flow curves for the two extreme temperatures, 145 °C and 482 °C, are shown in Figures 4 and 5. At 145 °C, the flow stress increases monotonically with strain and there is relatively little effect of strain rate. At 482 °C, and at all other test temperatures, the flow stress exhibits a maximum followed by flow softening. At those temperatures, the flow stress is highly strain-rate dependent.

No redundant work correction was applied to the average pressure. This seems to be justified by the experimental results of Dadras and Thomas on OFHC copper.[10] These results show that the relative difference in load for two widely different frictional conditions is approximately the same as the correction calculated from Eq. [1]. This difference in load includes both the frictional contribution *per se* and the redundant work contribution.

Temperature Correction. Because of deformation heating, the flow curves for $\dot{\varepsilon} > 10^{-2}\ s^{-1}$ do not correspond to isothermal conditions. Isothermal flow stress data, however, are desirable for process modeling. A temperature correction was therefore applied to the friction corrected data, as follows:

For each flow curve, the temperature increase due to deformation heating was calculated for each value of ε, using:

$$\Delta T(\varepsilon) = \frac{\eta}{\rho C_p} \int_0^{\varepsilon} \sigma d\varepsilon \qquad [2]$$

where ρ = specific gravity = 2.77 10^3 kg/m^3
C_p = heat capacity
η = efficiency of deformation heating[11]

Values of C_p for each test temperature were calculated from:

$$C_p(j/\text{kg K}) = -5.62 \times 10^{-9} T^3 + 2.44 \times 10^{-3} T^2 - 1.96T + 1.35 \times 10^{-3} \qquad [3]$$

where T is in K. Equation [3] was obtained by fitting published heat capacity data for Al-2024.[12] The integral in Eq. [2] was calculated from the (σ, ε) data pairs by using the trapezoid formula. The value of η was assumed to be independent of strain and was determined for each test by evaluating Eq. [2] at the end point of each friction-corrected flow curve. In calculating η from Eq. [2], the measured or estimated ΔT's at $\varepsilon = \varepsilon_f$ were used for the MTS tests. For the tests run on the Dake press, the estimated ΔT's at $\varepsilon \simeq 0.7$ were used. The estimated ΔT's were obtained using Figure 6. The ΔT and η values for the various test conditions are listed in Table II.

For each flow curve, the values of σ and of $T = T(\varepsilon = 0) + \Delta T(\varepsilon_i)$ were determined for strain values ε_i corresponding to regular strain increments (ε_i = 0.05, 0.1, 0.2, 0.3, 0.4, 0.5, 0.6) by linear interpolation between the two closest values of ε on each side of ε_i. For each value of ε_i, plots of log σ *vs* $1/T$ were then constructed for each strain rate. The plot for $\varepsilon_i = 0.3$, shown in Figure 7, is

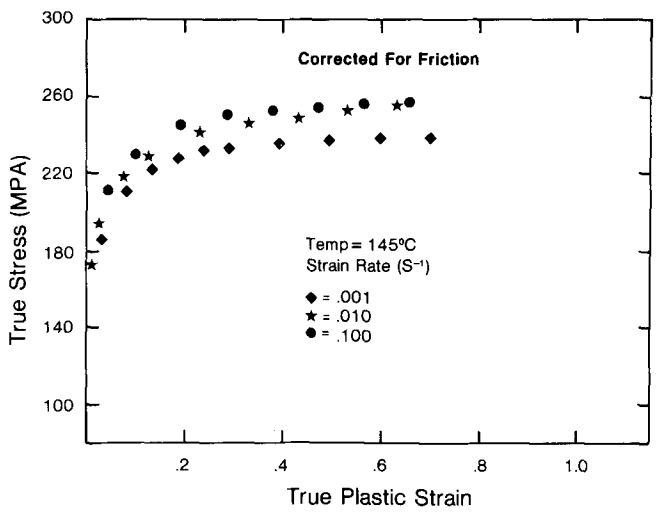

Fig. 4—Friction corrected flow curves for Al 2024-0 at $T = 145$ °C.

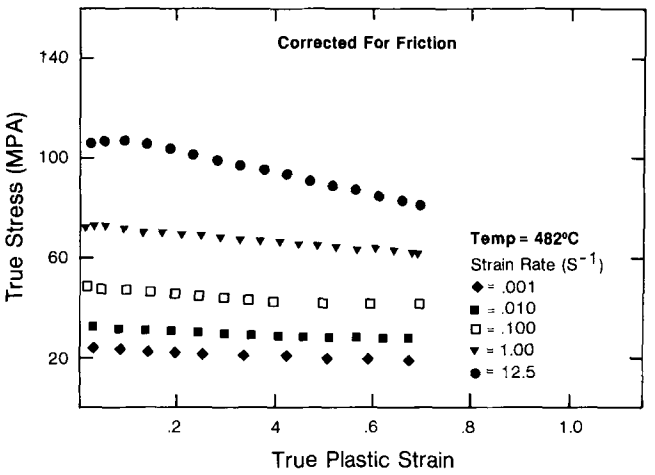

Fig. 5—Friction corrected flow curves for Al 2024-0 at $T = 482$ °C.

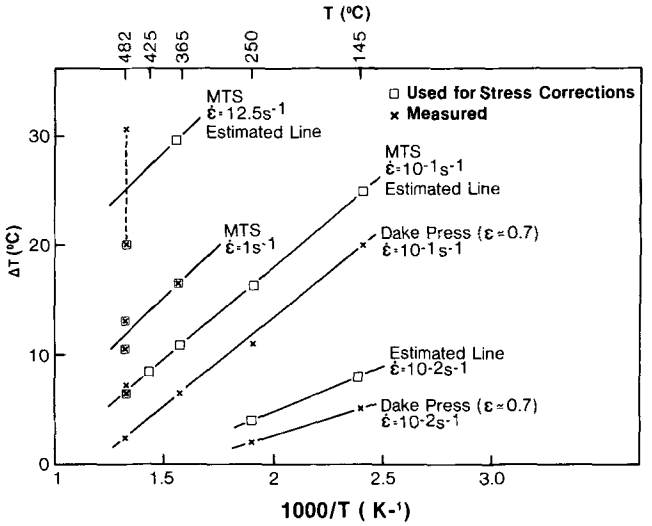

Fig. 6—Temperature increase, ΔT, at different test temperatures and strain rates.

Table II. Temperature Increase (ΔT) and Deformation Heating Efficiency (η) during "Isothermal" Compression of Al-2024-0

T (°C)	$\dot{\varepsilon}$ (s^{-1})	ΔT (°C)	η
145	10^{-2}	8	0.140
	10^{-1}	25	0.414
250	10^{-2}	4	0.173
	10^{-1}	16	0.517
365	10^{-1}	10.5	0.695
	1	16.5	0.777
	12.5	29.5	0.956
425	10^{-1}	8	0.675
482	10^{-1}	6.5	0.759
	1	11.7	0.880
	12.5	20	1.0

*At each temperature, ΔT and η were zero for all strain rates lower than those listed.

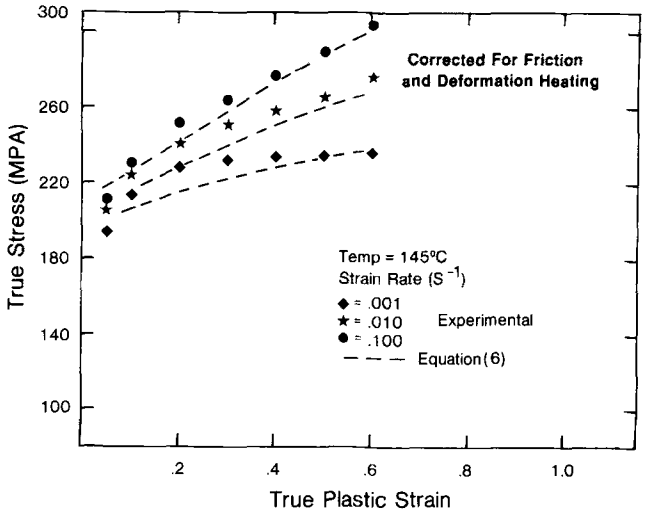

Fig. 8—Friction and temperature corrected flow curves for Al 2024-0 at 145 °C.

typical for all the strain levels; a bilinear or trilinear relation is observed between log σ and $1/T$. Equations were written for each linear segment for all strain rates and strains (ε_i's).

From these equations, the isothermal flow stress values were easily computed for each nominal test temperature, each strain rate, and each strain level (ε_i). At $\varepsilon = 0.6$, these flow stress values differed from the friction corrected flow stress data by 0 to 9.3 pct for all test conditions except one (T = 145 °C, $\dot{\varepsilon} = 10^{-1}\ s^{-1}$, $\Delta\sigma/\sigma$ = 19.4 pct). The resulting flow curves, corrected for friction and for deformation heating, are shown in Figures 8 to 12. When two tests were conducted at a given ($T, \dot{\varepsilon}$) combination, the average flow curve is shown. The strong effect of the temperature correction on the flow curves at 145 °C is evident by comparing Figures 4 and 8. At 250 °C and above, the temperature correction is smaller. In general, after correction, the flow curves still exhibit a maximum, followed by flow softening. The magnitude of the flow softening increases with increasing strain rate and, at a given strain rate, with decreasing temperature. Values of the peak stress, peak strain, and yield strength for the various test temperatures and strain rates are given in Table III.

B. *Strain Rate Dependence of the Flow Stress*

For each value of ε_i, plots of log σ *vs* log $\dot{\varepsilon}$ were made for the five nominal test temperatures using the final, corrected stress values. A typical plot is shown in Figure 13. An essentially linear relation is observed at all temperatures; *i.e.*, the strain rate sensitivity index, m, ($\sigma = K\,\dot{\varepsilon}^m|_{\varepsilon,T}$), is essentially independent of strain rate. This is true at all strain levels. Values of m and log K for the five test temperatures and the seven ε_i's, obtained from least square fits of the log σ *vs* log $\dot{\varepsilon}$ data, are listed in Table IV. The correlation coefficients, r, for most of these fits ranged from 0.995 to 0.9999. Only three, those corresponding to T = 145 °C and ε_i = 0.05, 0.1, and 0.6, were lower (r = 0.9875 to r = 0.9924). From Table IV, it is clear that m and K are strong functions of temperature but not of strain. The forms of the temperature dependence of m and log K for ε_i = 0.3 are shown in Figures 14 and 15, respectively.

In terms of the "efficiency of power dissipation", J/J_{max}, a parameter recently introduced to characterize the metallurgical material behavior under dynamic conditions,[4] the

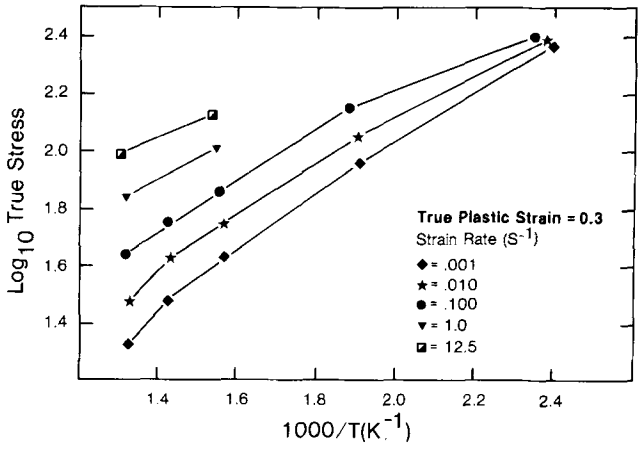

Fig. 7—Plot of log σ *vs* 1/T at different strain rates for ε = 0.3.

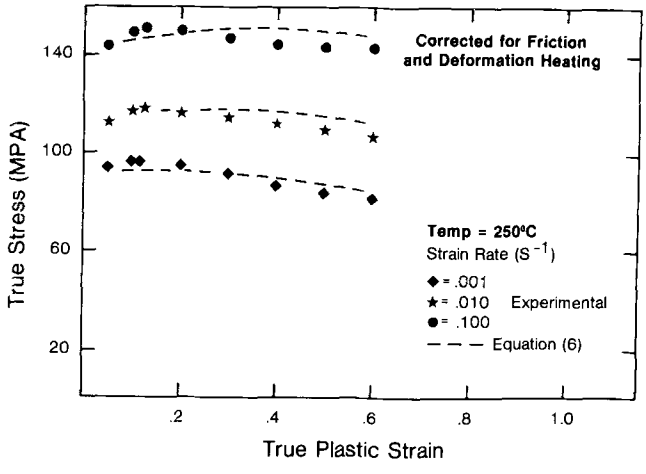

Fig. 9—Friction and temperature corrected flow curves for Al 2024-0 at 250 °C.

Table III. Peak Stress, σ_p, Peak Strain, ε_p, and Yield Strength, σ_y, during Isothermal Compression of Al-2024-0

T (°C)	$\dot{\varepsilon}$ (s^{-1})	σ_p (MPa)	ε_p	σ_y (MPa)
145	10^{-3}	no peak	no peak	90.6
	10^{-2}	no peak	no peak	137.7
	10^{-1}	no peak	no peak	154.2
250	10^{-3}	96.1	0.117	57.2
	10^{-2}	118.5	0.123	78.7
	10^{-1}	151.3	0.126	90.3
365	10^{-3}	45.8	0.048	36.8
	10^{-2}	59.3	0.052	53.3
	10^{-1}	78.4	0.069	68.7
	1	113.8	0.068	77.2
	12.5	149.8	0.046	144.4
425	10^{-3}	31.0	0.051	24.8
	10^{-2}	≃42.5	≃0.050	39.9
	10^{-1}	59.1	0.043	50.4
482	10^{-3}	≃23.5	≃0.050	19.6
	10^{-2}	32.1	0.069	28.9
	10^{-1}	48.3	0.023	45.2
	1	75.0	0.0375	66.7
	12.5	106.3	0.104	102.3

independence of m on strain rate results in constant efficiency contours ($J/J_{max} = 2m/(m+1)$ = constant) that are merely straight lines parallel to the strain rate axis in a temperature–strain rate representation. Values of J/J_{max}, calculated for $\varepsilon = 0.3$ using the values of m in Table IV, ranged from 0.055 at 145 °C to 0.29 at 482 °C. It should be noted that the values of J/J_{max} and therefore the shapes of the efficiency contours are quite sensitive to variations in m. For example, referring to Figure 13, if the slight departure from linearity of the log σ *vs* log $\dot{\varepsilon}$ plot at 482 °C is taken into account, resulting in $m = m(\dot{\varepsilon})$, and if m values are computed using a trilinear fit, one obtains values ranging from $m = 0.1425$ (for $\dot{\varepsilon} = 12.5\ s^{-1}$) to $m = 0.1854$ (for $\dot{\varepsilon} = 10^{-1}\ s^{-1}$) instead of the average value $m = 0.1697$. The corresponding values of J/J_{max} range from 0.25 to 0.32, instead of a constant value of 0.29, and therefore the constant efficiency contours are no longer straight lines near 482 °C.

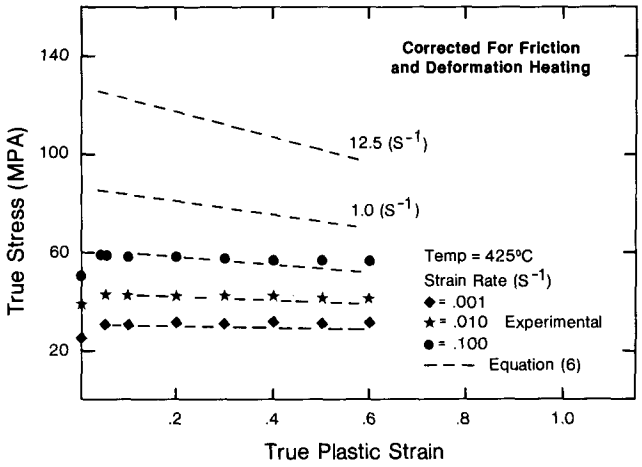

Fig. 11—Friction and temperature corrected flow curves for Al 2024-0 at 425 °C.

C. *Constitutive Equation*

To represent the flow stress in terms of ε, $\dot{\varepsilon}$, and T, the relation $\sigma = K\dot{\varepsilon}^m|_{\varepsilon,T}$ is a convenient starting point since m is essentially independent of strain rate. Then, for each strain, ε_i, m and K are expressed as functions of temperature by fitting a cubic to the data pairs $(m, T)_{\varepsilon_i}$ and a cosine to the points $(\log K, T)_{\varepsilon_i}$:

$$m = AT^3 + BT^2 + CT + D \quad [4]$$

$$\log K = a\cos[b(T-c)] + d \quad [5]$$

Because m and K do not vary strongly with strain, Eqs. [4] and [5] are applicable to all strain levels, but with somewhat different coefficients. These coefficients, which are given in Table V, were plotted *vs* ε_i and fitted by linear expressions of the type:

$$\text{coefficient} = \alpha\varepsilon + \beta$$

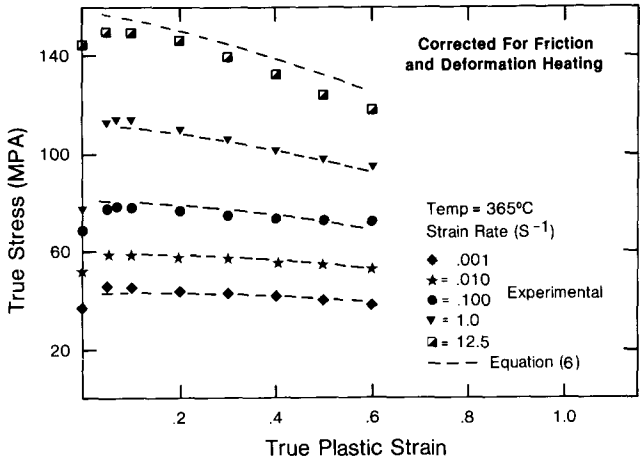

Fig. 10—Friction and temperature corrected flow curves for Al 2024-0 at 365 °C.

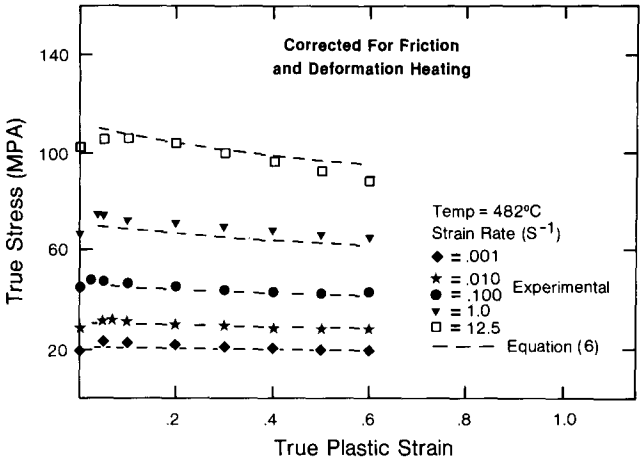

Fig. 12—Friction and temperature corrected flow curves for Al 2024-0 at 482 °C.

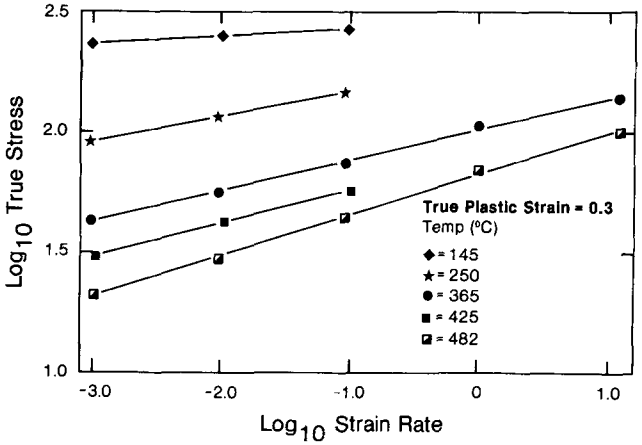

Fig. 13—Plot of log σ *vs* log $\dot{\varepsilon}$ for the five test temperatures at $\varepsilon = 0.3$.

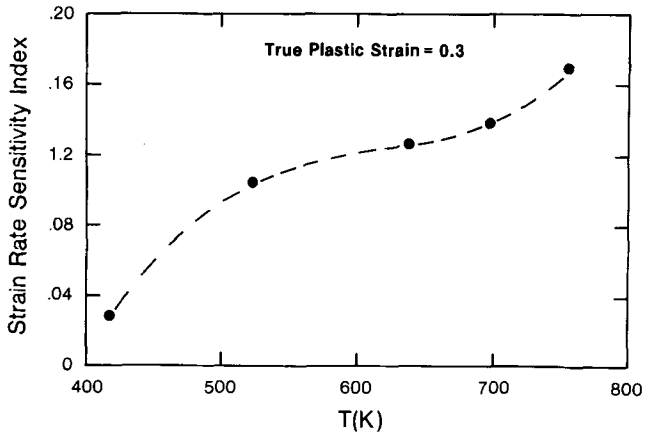

Fig. 14—Plot of strain rate sensitivity index, m, *vs* T for $\varepsilon = 0.3$.

The correlation coefficients for these fits ranged from 0.984 to 0.988 for A, B, C, D and from 0.911 to 0.967 for a, b, c, d.

In summary, for the range of variables $0.05 \leqq \varepsilon \leqq 0.6$, $10^{-3}\ s^{-1} \leqq \dot{\varepsilon} \leqq 12.5\ s^{-1}$, and 145 °C $\leqq T \leqq$ 482 °C, the following constitutive equation represents the flow behavior:

$$\sigma = K(T, \varepsilon)\dot{\varepsilon}^{m(T,\varepsilon)} \qquad [6]$$

with:

$$\log K(T, \varepsilon) = a \cos[b(T - c)] + d$$

$$a = 0.1997\varepsilon + 0.2715$$

$$b = 0.0456\varepsilon + 0.4160$$

$$c = -90\varepsilon + 412.5$$

$$d = 0.1952\varepsilon + 2.0660$$

$$m(T, \varepsilon) = AT^3 + BT^2 + CT + D$$

$$A = 1.55 \times 10^{-8}\varepsilon + 5.7 \times 10^{-9}$$

$$B = -2.653 \times 10^{-5}\varepsilon - 1.096 \times 10^{-5}$$

$$C = 0.01445\varepsilon + 0.00730$$

$$D = -2.4720\varepsilon - 1.5391 \qquad [7]$$

Table IV. Strain Rate Sensitivity Index, m, and Log K, from $\sigma = K\dot{\varepsilon}^m$, for Al-2024-0 at Various Temperatures and Strains

Temperature (°C)	Strain						
	0.05	0.1	0.2	0.3	0.4	0.5	0.6
145	m = 0.0184	0.0168	0.0218	0.0281	0.0364	0.0456	0.0552
	log K = 2.345	2.381	2.424	2.452	2.482	2.511	2.543
250	0.0949	0.0976	0.1016	0.1047	0.1125	0.1191	0.1239
	2.252	2.274	2.279	2.275	2.279	2.282	2.283
365	0.1283	0.1297	0.1298	0.1267	0.1250	0.1220	0.1201
	2.037	2.038	2.027	2.010	1.993	1.976	1.961
425	0.1426	0.140	0.1396	0.1392	0.1350	0.1332	0.1314
	1.914	1.905	1.903	1.899	1.889	1.885	1.881
482	0.1648	0.1664	0.1692	0.1697	0.1699	0.1684	0.1674
	1.851	1.847	1.837	1.824	1.812	1.799	1.789

Table V. Coefficients of $m(T, \varepsilon)$ and Log $K(T, \varepsilon)$ in Equations [4] and [5]

ε	$10^9 \times A$	$10^5 \times B$	$10^3 \times C$	D	a	b	c	d
0.05	6.18	−1.176	7.668	−1.584	0.3	0.42	410	2.05
0.1	7.74	−1.452	9.276	−1.888	0.28	0.42	400	2.1
0.2	8.87	−1.643	10.305	−2.063	0.31	0.42	400	2.11
0.3	9.51	−1.747	10.823	−2.138	0.32	0.43	380	2.14
0.4	12.51	−2.262	13.676	−2.640	0.35	0.44	365	2.15
0.5	13.43	−2.423	14.541	−2.780	0.37	0.44	370	2.15
0.6	14.94	−2.674	15.860	−2.994	0.40	0.44	360	2.18

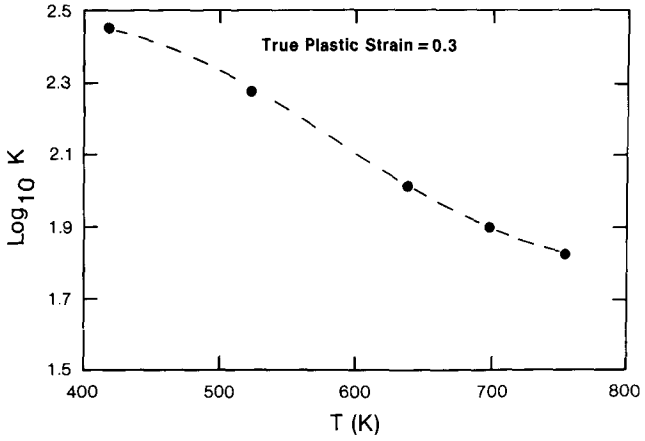

Fig. 15—Plot of log K (from $\sigma = K\dot{\varepsilon}^m$) *vs* T for $\varepsilon = 0.3$.

The flow curves predicted from Eq. [6] are generally in very good agreement with the experimental data for 365 °C $\leqq T \leqq$ 482 °C (Figures 10 to 12). At lower temperatures, T = 250 °C and especially 145 °C, the agreement is somewhat less good (Figures 8 and 9).

D. *Temperature Dependence of the Flow Stress and Activation Energies*

At constant strain and strain rate, the variation of σ with T can be obtained from Eqs. [6] and [7]. The forms of these equations, however, do not permit direct calculation of activation energies for the flow softening processes. Yet, a knowledge of the activation energies can indicate what mechanisms operate during flow softening. One commonly used method to determine activation energies is based on the assumption that the combined temperature and strain rate dependence of the flow stress can be represented by the functional dependence:

$$\sigma_\varepsilon = \sigma_\varepsilon\left[\dot{\varepsilon}\exp\left(\frac{\Delta H}{RT}\right)\right] \qquad [8]$$

where σ_ε is the flow stress at constant strain, ΔH is an activation energy, and $\dot{\varepsilon}\exp(\Delta H/RT)$ is the Zener-Hollomon parameter. A plot of log $\dot{\varepsilon}$ *vs* $1/T$ at constant σ_ε is linear if the previous assumption is satisfied and in this case ΔH is easily obtained from the slope.

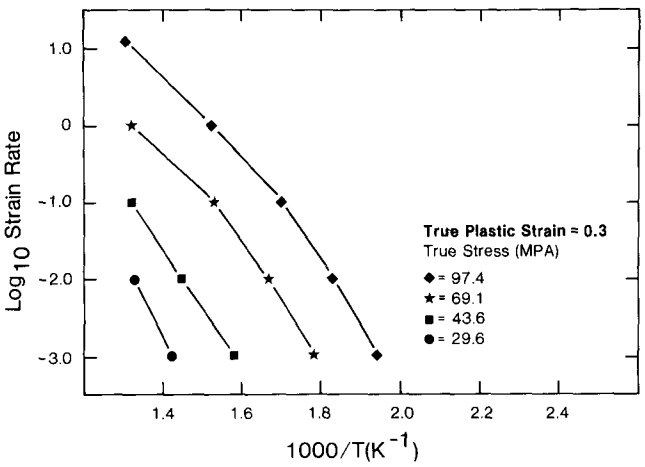

Fig. 16—Plot of log $\dot{\varepsilon}$ *vs* $1/T$ for several constant values of stress.

With the present data such plots, shown in Figure 16, are not linear over the whole range of temperatures and therefore values of ΔH can be calculated only between consecutive points. These values of ΔH range from 22 to 48.5 Kcal/mole for the various strain rates and temperatures. The lower values of ΔH correspond to the higher temperatures and strain rates.

Because ΔH is temperature and strain rate dependent, the Zener-Hollomon parameter and Eq. [8] do not provide a suitable modeling approach for the flow behavior of this material.[13] The model proposed in Eq. [6] is preferable. However, it is interesting to note that the range of ΔH values obtained includes the activation energies for aluminum self-diffusion (30.5 to 34 Kcal/mole) and for hetero-diffusion of copper in aluminum (31 to 42 Kcal/mole).[14] The first mechanism would occur during recovery, when dislocation climb is involved. The second mechanism would occur during dissolution of the $CuMgAl_2$ precipitate, resulting in softening. During recovery, cross-slip would also occur. Activation energies for cross-slip, however, appear less well known than those for diffusion.[15,16]

E. *As-Deformed Microstructures*

As-deformed microstructures were examined to try to correlate the changes in flow stress behavior with microstructural changes. In this examination, care was exercised to avoid the corners of the specimens and the dead zones where the strains deviate significantly from the average strain.

After deformation at 145, 250, and 365 °C and at strain rates of 10^{-3} to 10^{-1} s^{-1}, the microstructures were similar in spite of the large differences in flow stress level and in stress-strain behavior. The effect of the compression was evident; *i.e.*, in comparison with the as-annealed microstructures, the grains were distorted, less elongated, and the grain boundaries had lost their straightness (Figures 17(a) and (b)).

Compression at 425 °C, the annealing temperature, resulted in a gradual change in microstructure, which increased with increasing strain rate. In these specimens, the grain boundaries were more easily etched than in the specimens compressed at lower temperatures (Figures 17(b) and (c)). Although evidence of the initial, elongated microstructure was retained, many transverse subgrains were seen (Figure 18). Also, at the highest strain rate ($\dot{\varepsilon} = 10^{-1}$ s^{-1}), very fine equiaxed grains were seen in local regions near the alignments of (Cu, Al) particles (Figure 19), indicating that either static or dynamic recrystallization had occurred, presumably because of the locally higher strain and strain rate in the vicinity of the particles.

After compression at 482 °C, which, because of deformation heating, resulted in final test temperatures above the solution temperature (493 °C) for $\dot{\varepsilon} = 1$ s^{-1} and above the solidus temperature (502 °C) for $\dot{\varepsilon} = 12.5$ s^{-1}, some distinctly different microstructures were observed, which, in some cases, contained numerous regions of fine, equiaxed grains (5 to 15 μm in diameter). At the lower strain rates (10^{-3} to 10^{-1} s^{-1}), the microstructures were similar to those observed for T = 425 °C, $\dot{\varepsilon} = 10^{-1}$ s^{-1}, except that the

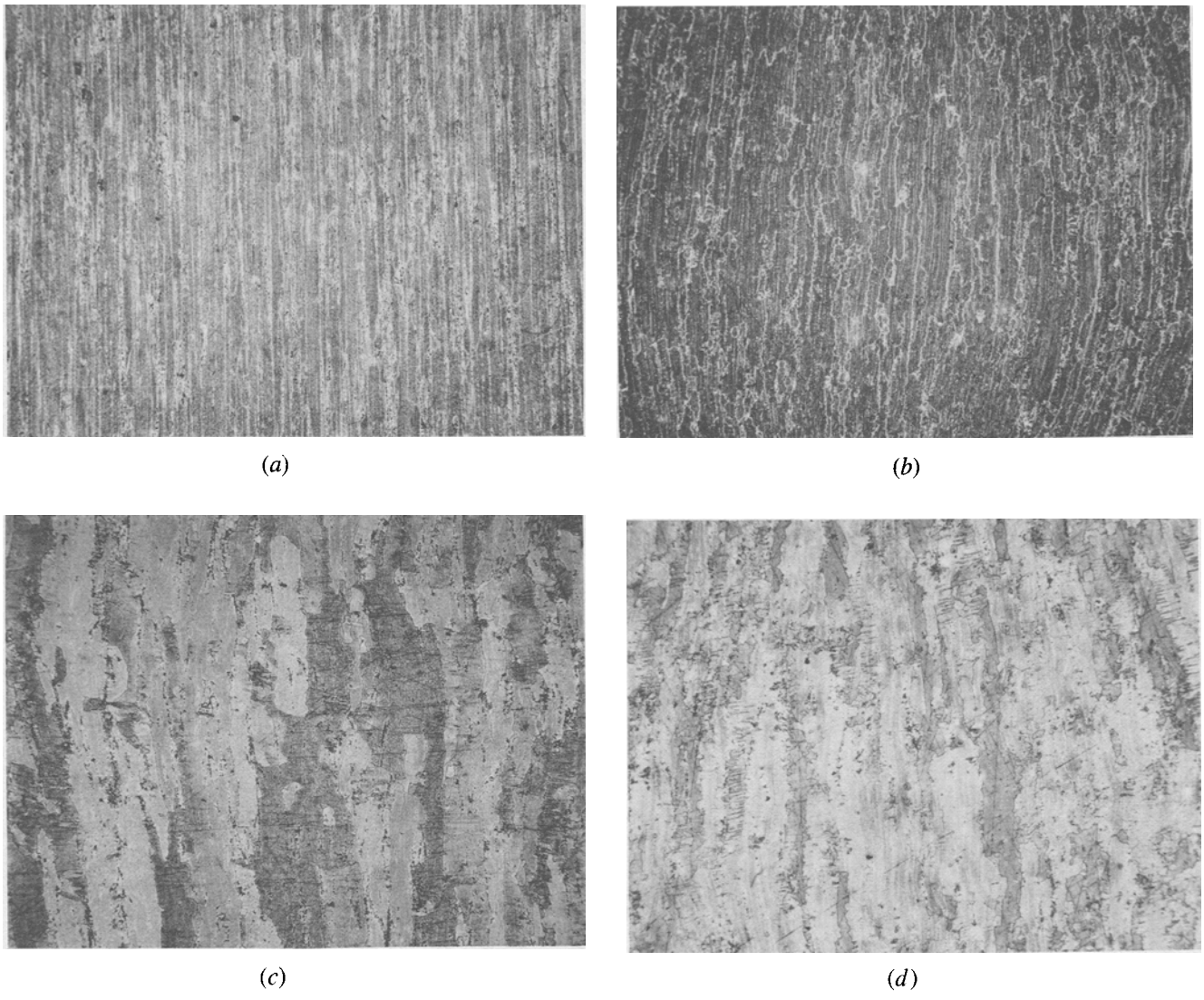

Fig. 17 — Typical microstructures of Al 2024-0 before and after hot compression to $\varepsilon \simeq 0.8$. (*a*) As-annealed. (*b*) 250 °C, $\dot{\varepsilon} = 10^{-1}\ s^{-1}$. (*c*) 425 °C, $\dot{\varepsilon} = 10^{-1}\ s^{-1}$. (*d*) 482 °C, $\dot{\varepsilon} = 12.5\ s^{-1}$. Magnification 26 times.

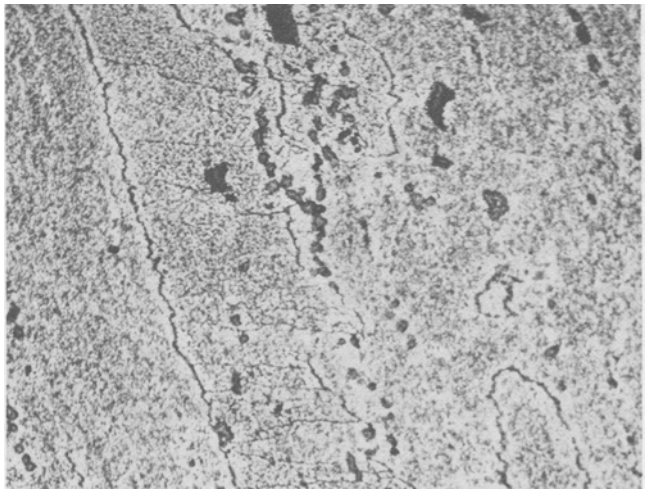

Fig. 18 — Subgrains in Al 2024-0 compressed to $\varepsilon \simeq 0.8$ at $T = 425$ °C, $\dot{\varepsilon} = 10^{-2}\ s^{-1}$. Compression axis vertical. Magnification 296 times.

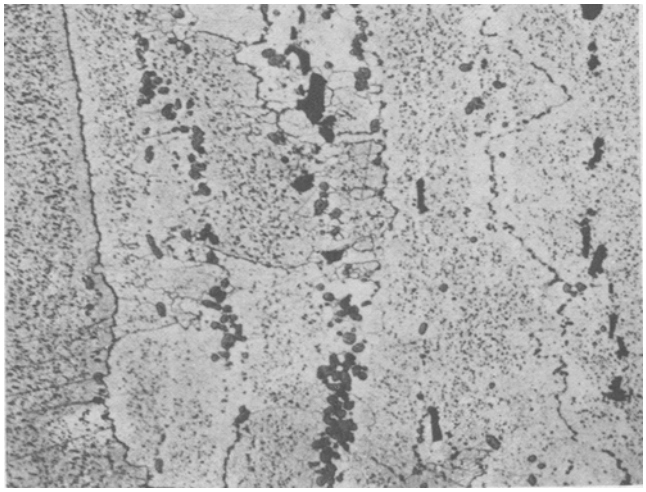

Fig. 19 — Fine, equiaxed grains in Al 2024-0 after compression to $\varepsilon \simeq 0.8$ at $T = 425$ °C, $\dot{\varepsilon} = 10^{-1}\ s^{-1}$. Magnification 296 times.

precipitate was less abundant due to partial dissolution resulting from the higher temperature. For $\dot{\varepsilon} = 1$ and 12.5 s^{-1}, a banded structure consisting of thin grains transverse to the compression axis was observed within many of the large elongated grains (Figure 17). These transverse grains appeared to have formed by lateral growth of the fine, equiaxed grains nucleated near the (Cu, Al) particles (Figure 20). In one of the specimens, in which the temperature observed at the end of the test was 10 °C above the solidus temperature, fine equiaxed grains were present at most of the initial grain boundaries and there was evidence of melting in these regions (Figure 21).

IV. SUMMARY AND CONCLUSIONS

1. Hot compression tests on Al 2024-0 at temperatures of 145 to 482 °C and at constant true strain rates of 10^{-3} to 12.5 s^{-1} have been performed to obtain isothermal flow stress data. Analysis included a friction correction, in which interfacial friction factors estimated from ring tests were used, and a temperature correction, which accounted for deformation heating.
2. At 250 °C and above, the isothermal flow curves generally exhibited a maximum followed by flow softening. At a given temperature, the amount of softening ($\Delta\sigma$) increased with increasing strain rate. At a given strain rate, $\Delta\sigma$ increased with decreasing temperature. At 145 °C, the flow curves exhibited strain hardening.
3. In the temperature and strain rate ranges 250 °C $\leqq T \leqq$ 482 °C and 10^{-3} $s^{-1} \leqq \dot{\varepsilon} \leqq$ 12.5 s^{-1}, and for strains less than 0.6, the flow behavior of Al 2024-0 can be represented by a constitutive equation of the form

$$\sigma = K(T, \varepsilon)\dot{\varepsilon}^{m(T,\varepsilon)}$$

where K and m are strong functions of temperature but not of strain; log K and m are simple trigonometric and polynomial functions of T and ε.
4. Metallographic examination of the as-deformed microstructures generally supports the idea that flow softening in Al 2024-0 is associated with dynamic recovery. Also, at the highest temperature (482 °C), there was evidence of redissolution of the precipitate. Fine recrystallized grains were observed at 425 °C and 482 °C for $\dot{\varepsilon} \geqq$ 0.1 s^{-1}, but only in local areas, near second phase particles, or at the as-annealed grain boundaries.

Fig. 20 — Elongated "grains" transverse to the compression axis in Al 2024-0 compressed to $\varepsilon \simeq 0.7$ at 482 °C, $\dot{\varepsilon} = 12.5$ s^{-1}. Compression axis vertical. Magnification 388 times.

(*a*)

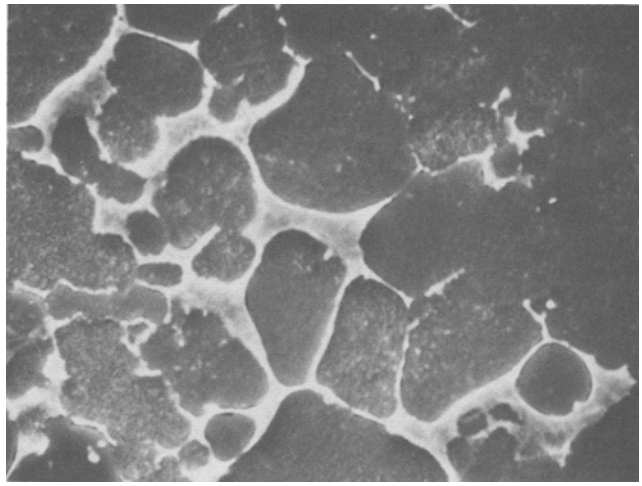

(*b*)

Fig. 21 — Fine, equiaxed grains along the primary, as-annealed grain boundaries in Al 2024-0 compressed to $\varepsilon \simeq 0.7$ at 482 °C, $\dot{\varepsilon} = 12.5$ s^{-1}. Magnification of (*a*) 74 times and (*b*) 1480 times.

ACKNOWLEDGMENTS

This work was supported by the United States Air Force Materials Laboratory under Contract Number F33615-78-C-5025 to Battelle Columbus Laboratories, Dr. H. L. Gegel, Project Director, through a sub-contract from Battelle. The authors thank Dr. S. L. Semiatin, BCL, for arranging and supervising the high strain rate tests ($\dot{\varepsilon}$ = 1 and 12.5 s^{-1}).

REFERENCES

1. G. D. Lahoti, S. L. Semiatin, S. I. Oh, T. Altan, and H. L. Gegel: *Advanced Processing Methods for Titanium*, D. F. Hasson and C. H. Hamilton, eds., TMS-AIME, 1982, pp. 23-39.
2. S. L. Semiatin, S. I. Oh, and T. Altan: Technical Report AFWAL-TR-83-4109, AFWAL Materials Laboratory, WP-AFB, OH 45433, 1985.
3. R. Raj: *Metall. Trans. A*, 1981, vol. 12A, pp. 1089-97.
4. Y. V. R. K. Prasad, H. L. Gegel, S. M. Doraivelu, J. C. Malas, J. T. Morgan, K. A. Lark, and D. R. Barker: *Metall. Trans. A*, 1984, vol. 15A, pp. 1883-92.
5. Y. V. R. K. Prasad: private communication, AFWAL Materials Laboratory, WP-AFB, OH 45433, 1984.
6. P. Dadras and W. R. Wells: Trans. ASME, *Journal of Engineering for Industry*, 1984, vol. 106, pp. 187-95.
7. S. L. Semiatin and G. D. Lahoti: *Metall. Trans. A*, 1981, vol. 12A, pp. 1705-17.
8. A. T. Male and M. G. Cockcroft: *J. Inst. Metals*, 1964, vol. 93, pp. 38-46.
9. V. DePierre and A. T. Male: Technical Report AFML-TR-69-28, AFWAL Materials Laboratory, WP-AFB, OH 45433, 1969.
10. P. Dadras and J. F. Thomas, Jr.: *Compression Testing of Homogeneous Materials and Composites*, R. Chait and R. Papirno, eds., ASTM, 1983, pp. 24-39.
11. P. Dadras and J. F. Thomas, Jr.: *Metall. Trans. A*, 1981, vol. 12A, pp. 1867-76.
12. A. Goldsmith, T. E. Waterman, and H. J. Hirschhorn: *Handbook of Thermophysical Properties of Solid Materials*, MacMillan, New York, NY, 1961, vol. 2, p. 755.
13. W. J. McGregor Tegart: *Elements of Mechanical Metallurgy*, MacMillan, New York, NY, 1966, p. 43.
14. Y. Adda and J. Philibert: *La Diffusion dans les Solides*, Presses Universitaires de France, Paris, 1966, vol. II, pp. 1129 and 1149.
15. J. Friedel: *Dislocations*, Addison-Wesley, Reading, MA, 1964.
16. B. Escaig: *Dislocation Dynamics*, A. R. Rosenfield, G. T. Hahn, A. L. Bement, and R. I. Jaffee, eds., McGraw-Hill, New York, NY, 1968, pp. 653-77.